



A comprehensive study of structure and properties of nanocrystalline zinc peroxide

Dmitry Bocharov^{a,*}, Andrei Chesnokov^a, George Chikvaidze^a, Jevgenijs Gabrusenoks^a, Reinis Ignatans^b, Robert Kalendarev^a, Matthias Krack^c, Karlis Kundzins^a, Alexei Kuzmin^a, Nina Mironova-Ulmane^a, Inga Pudza^a, Laurits Puust^d, Ilmo Sildos^d, Evgeni Vasil'chenko^{a,d}, Martins Zubkins^a, Juris Purans^{a,**}

^a Institute of Solid State Physics, University of Latvia, Kengaraga Street 8, LV-1063, Riga, Latvia

^b Institute of Materials, École polytechnique fédérale de Lausanne, Station 12, Lausanne, Switzerland

^c Paul Scherrer Institute, Forschungsstrasse 111, CH-5232, Villigen PSI, Switzerland

^d Institute of Physics, University of Tartu, W. Ostwald Street 1, 50411, Tartu, Estonia

ARTICLE INFO

Keywords:

ZnO₂
X-ray diffraction
X-ray absorption spectroscopy
Infrared spectroscopy
Raman spectroscopy
First-principles calculations

ABSTRACT

Nanocrystalline zinc peroxide (nano-ZnO₂) was synthesized through a hydrothermal process and comprehensively studied using several experimental techniques. Its crystal structure was characterized by X-ray diffraction, and the average crystallite size of 22 nm was estimated by Rietveld refinement. The temperature-dependent local environment around zinc atoms was reconstructed using reverse Monte Carlo (RMC) analysis from the Zn K-edge X-ray absorption spectra. The indirect band gap of about 4.6 eV was found using optical absorption spectroscopy. Lattice dynamics of nano-ZnO₂ was studied by infrared and Raman spectroscopy. *In situ* Raman measurements indicate the stability of nano-ZnO₂ up to 250 °C above which it decomposes into ZnO and O₂. The obtained experimental results were supported by first-principles density functional theory (DFT) calculations.

1. Introduction

Zinc peroxide (ZnO₂) is a wide-band gap semiconductor that has been attracting the attention of scientists for several decades. It has many applications across a variety of industries: it is used by the rubber industry [1]; it is used in the production of plastics [2], in cosmetics and pharmacy [3]; it is an oxidant for explosives and pyrotechnic mixtures [4], and a precursor to ZnO [5–14]; it is a photocatalyst [15,16], a luminophore [17,18]; it can be used to purify water [19] and as a detoxification agent against mustard gas [20]. Recently, antibacterial and antiviral properties of ZnO₂ nanoparticles were also reported [21,22]. A progress report by Hu et al. published in 2021 summarizes and discusses the advances in the construction of versatile metal peroxide nanoparticles for disease-specific chemoreactive nanotherapeutics [23]. Finally, zinc peroxide was mentioned as a prospective material for rechargeable zinc-air batteries [24].

The phase transition of hexagonal ZnO into cubic ZnO₂ induced by hydrogen peroxide treatment on the surface of ZnO switching memory

film is a prospective approach for making fully transparent analog memristor devices [25].

The reverse process of mechanochemical transformation of ZnO₂ into a highly defective ZnO was also discussed in the literature [26]. The production of a stable *p*-type ZnO phase remains a research goal in the development of ZnO-based optoelectronic devices, and ZnO₂ appears to be a suitable precursor to achieve a Zn-poor ZnO, which is a phase favorable towards *p*-type conductivity [9,27].

To our knowledge, zinc peroxide has never been synthesized as a single-crystal and exists at ambient pressure in nanocrystalline (2–100 nm) form of cubic-ZnO₂. A principal strategy for obtaining ZnO₂ nanoparticles is to oxidize reactive Zn species with hydrogen peroxide. However, the exact procedure (Zn-containing reactant, reaction temperature, stirring time, reaction medium, etc.) varies across sources and only in few cases pure nanocrystalline ZnO₂ was obtained, while in many cases the products are a mixture of zinc peroxide and zinc oxide in different forms. Reaction temperatures range from ambient [8,28] to 100 °C and beyond [5,17,18]. Active Zn species are generated from either zinc oxide [17,18,28] or zinc acetate [5,7,29–31]. More exotic

* Corresponding author.

** Corresponding author.

E-mail addresses: bocharov@cfi.lu.lv (D. Bocharov), purans@cfi.lu.lv (J. Purans).

methods involve converting inorganic zinc salts into zinc-organic compounds [32,33], or even laser ablation of metallic zinc [6].

In contrast to ZnO₂ nanoparticles, few studies are dedicated to ZnO₂ thin films. Successive ionic layer adsorption and reaction (SILAR) techniques [10], electrochemical deposition [34], ZnO chemical conversion [35], as well as magnetron deposition at cryogenic temperature substrates [36] have been used to obtain ZnO₂ thin films.

The structural, optical, vibrational properties of ZnO₂ have been studied in the past by different experimental methods such as X-ray diffraction, X-ray absorption (XAFS), Scanning and Transmission electron microscopy (SEM, TEM), UV/VIS optical, Raman/IR and photoluminescence spectroscopies [7,11,29–31,36–39]. Cubic ZnO₂ has a pyrite structure (space group $Pa\bar{3}$ (No. 205), $a = 4.871 \text{ \AA}$ [40]) with peroxide (O₂)²⁻ groups being shared between two neighbouring ZnO₆ octahedra (Fig. 1) [9,32,41,42]. Peroxide bond length is 1.47 Å, being significantly shorter than the bond length between zinc and oxygen ions (2.11 Å). A large difference in electronegativity between zinc and oxygen atoms suggests a predominantly ionic bond character [11].

Upon heating at ambient pressure, ZnO₂ decomposes into hexagonal ZnO phase ($2\text{ZnO}_2(\text{s}) \rightarrow 2\text{ZnO}(\text{s}) + \text{O}_2(\text{g})$) with an exothermic peak around 200–230 °C [13,43]. If the size of ZnO₂ nanocrystals decreases down to 2–3 nm, the transition occurs in a broader temperature range (180–250 °C) as demonstrated by in-situ XRD and EXAFS measurements [32,39]. Moreover, a presence of an intermediate amorphous phase at the transition process [39] is suggested. The relatively low decomposition temperature is caused by unstable peroxide groups and local charge imbalance in the ZnO₂ structure [9,11]. However, at room temperature, ZnO₂ is stable under a pressure up to 36 GPa [32].

The number of theoretical studies of ZnO₂ is still limited. Bulk modulus, band structure, and electronic density of states were calculated in Ref. [32] using the LDA approximation and plane-wave basis set. Magnetic, elastic, and optical properties of ZnO₂ were calculated using a plane-wave basis set with different functionals by Thapa et al. [44]. First-principles calculations predict the existence of dynamically and mechanically stable two-dimensional pentagonal ZnO₂ phase [45–47] as well as a ZnO₂ phase with $I4/mcm$ space group (No. 140) [48,49], which becomes thermodynamically stable only above 120 GPa [50].

The experimentally reported band gap of ZnO₂ is in the range between 3.4 eV and 4.6 eV [30,32,41] and has indirect character with the valence band maximum located at Γ and with the conduction band minimum located between Γ and R points of the Brillouin zone [32]. First-principle calculations within the density functional theory (DFT) showed that there is a strong hybridization between Zn-d and O-p states in the valence band [32].

The dispersion in the structural, optical, and vibrational properties of nanocrystalline ZnO₂ comes from the nanocrystal sizes, morphology,

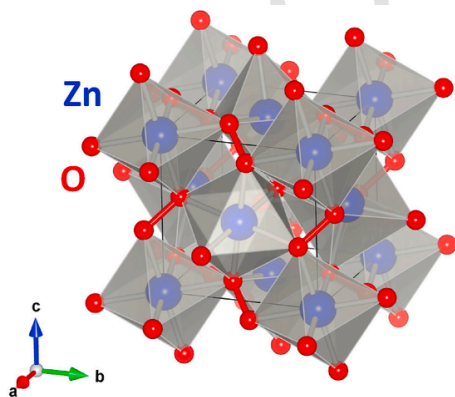


Fig. 1. Crystallographic structure of ZnO₂. The bonds between two oxygen ions forming O₂²⁻ anions are shown by red bars. (For interpretation of the references to colour in this figure legend, the reader is referred to the Web version of this article.)

and stoichiometry of zinc peroxide nanoparticles. Moreover, the mixed-phase compounds of ZnO₂ and ZnO or core-shell structure of ZnO₂/ZnO lead to a broader dispersion of the properties of studied samples. In contrast to ZnO, where point defects and defects induced by disordering are very well studied [51,52], the role of disorder and defects in the structure of ZnO₂ is still largely unknown. Therefore, before ZnO₂ nanoparticles or thin films can be adopted for the next advanced applications, it is necessary to establish their exact local structure, as well as obtain a complete understanding of the contribution of disorder.

In the present work, we have carried out a systematic and comprehensive study of the properties of ZnO₂ nanoparticles by several experimental methods using the same sample. The local structure and lattice dynamics of ZnO₂ nanoparticles have been studied for the first time using synchrotron radiation X-ray absorption spectroscopy combined with advanced analysis based on reverse Monte-Carlo (RMC) simulations. The combination of experimental methods allowed us to carry out a multiscale study of ZnO₂: XAFS (short-range), Raman scattering (medium-range), and XRD concomitantly with SEM morphological imaging (long-range), similarly to a recent study [53].

2. Experimental

Nanocrystalline ZnO₂ (nano-ZnO₂) powders were produced by a hydrothermal process using zinc acetate as a precursor and hydrogen peroxide as an oxidizing agent. 11.4 g of zinc acetate dihydrate ($\text{Zn}(\text{CH}_3\text{COO})_2 \cdot 2\text{H}_2\text{O}$, Sigma-Aldrich, 99.999%) were dissolved in 750 ml of deionized water in a round-bottom flask with a dephlegmator and 70 ml of hydrogen peroxide (H₂O₂; mol.30%). The solution was heated up to 100 °C to conduct the hydrothermal reaction. Afterward, the solution was cooled down to room temperature, and ZnO₂ powder was extracted from the liquid and washed with deionized water. The material was finally dried in the air for 24 h.

The crystallographic structure and crystallite size of nano-ZnO₂ were determined by the X-ray diffraction (XRD) technique. XRD measurements were performed using a PANalytical X'Pert PRO diffractometer equipped with the Cu ($K\alpha$) anode X-ray tube and a multichannel solid-state detector. The X-ray tube operated at 45 kV and 40 mA. The diffraction pattern was recorded in the range of $2\theta = 10\text{--}140^\circ$ with a step size of $\Delta(2\theta) = 0.0263^\circ$.

The morphology and sizes of ZnO₂ nanoparticles were investigated by scanning electron microscope (SEM) Tescan Lyra3, equipped with a high brightness Schottky emitter. SEM images were taken using beam accelerating voltage 15 kV and beam current 100 pA.

The local atomic structure of nano-ZnO₂ powder was studied using the X-ray absorption spectroscopy at the HASYLAB/DESY PETRA-III P65 Applied XAFS beamline [54]. The PETRA-III storage ring operated at $E = 6.08 \text{ GeV}$ and current $I = 95 \text{ mA}$ in top-up 40 bunch mode. Temperature-dependent X-ray absorption spectra were recorded at the Zn K-edge in transmission mode using two ionization chambers located before and after the sample. The X-ray beam from an undulator was monochromatized using a fixed-exit Si(111) double-crystal monochromator. The harmonic rejection was achieved by an uncoated silicon plane mirror. An Oxford Instruments liquid helium flow cryostat was used to maintain the sample temperature in the range of 10–300 K. The sample was prepared from ZnO₂ powder, which was gently milled in an agate mortar and deposited on a Millipore membrane. The sample thickness was adjusted to give the value of the absorption edge jump $\Delta\mu = 1$.

Optical properties of nano-ZnO₂ powder were studied by a JASCO V-660 UV/VIS double-beam spectrophotometer equipped with deuterium and tungsten iodine lamps in the range of 200–800 nm at room temperature with an optical resolution of 1.0 nm.

Optical absorption spectra were measured on UV-Vis spectrometer Jasco V-660. The V-660 is a double-beam spectrophotometer utilizing a double monochromator and a photomultiplier tube detector. Spectra of

the ZnO₂ nanopowders were recorded at room temperature in the wavelength range of 200–800 nm with a scan rate of 5 nm/s and resolution of 1.0 nm at room temperature. CaF₂ was used in the measurements as a substrate and reference.

Vibrational properties were characterized using FTIR and Raman spectroscopies. A vacuum Fourier transform infrared spectrometer Bruker VERTEX 80v was used to measure the infrared spectrum of a pellet in the energy range 50–600 cm⁻¹ where theoretically predicted IR peaks lie. The pellet was prepared from mechanically mixed nano-ZnO₂ and KBr powders, and then the mixture was compressed using a standard KBr pellet method. Note that the long-wavelength border of the spectrum is limited to 200 cm⁻¹ due to the border of the transparency of the pellet. Temperature-dependent Raman scattering spectra were collected by a Renishaw micro-Raman spectrometer under the excitation at 514.5 nm. The sample temperature was controlled by the Linkam THMS350V stage. The optical chamber was weakly blown through with 99.999% purity nitrogen during the measurements.

3. Results

3.1. X-ray diffraction and SEM

X-ray diffraction pattern of nano-ZnO₂ (Fig. 2) does not contain any impurity phases. All peaks can be assigned to the ZnO₂ phase with a *Pa* $\bar{3}$ (No. 205) space group. Initial lattice parameters and atomic coordinates for the Rietveld refinement were taken from Ref. [32]. Rietveld refinement was performed with the BGMN [55] software using the Prox code [56] and resulted in a very good fit. Some discrepancies be-

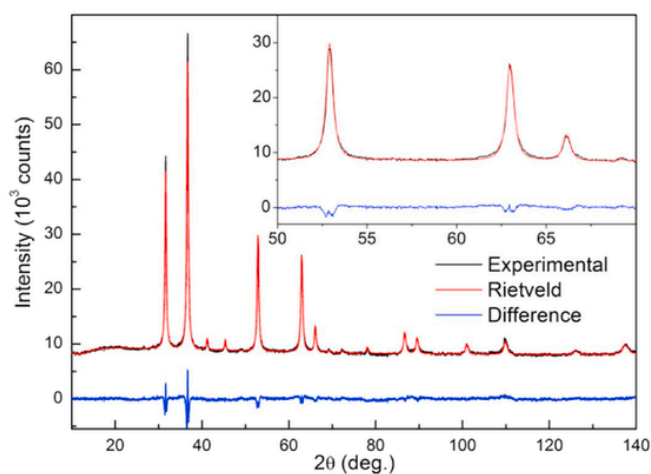


Fig. 2. Experimental and calculated diffraction patterns of nano-ZnO₂; inset shows the enlarged part of the diffraction pattern between 50° and 70°.

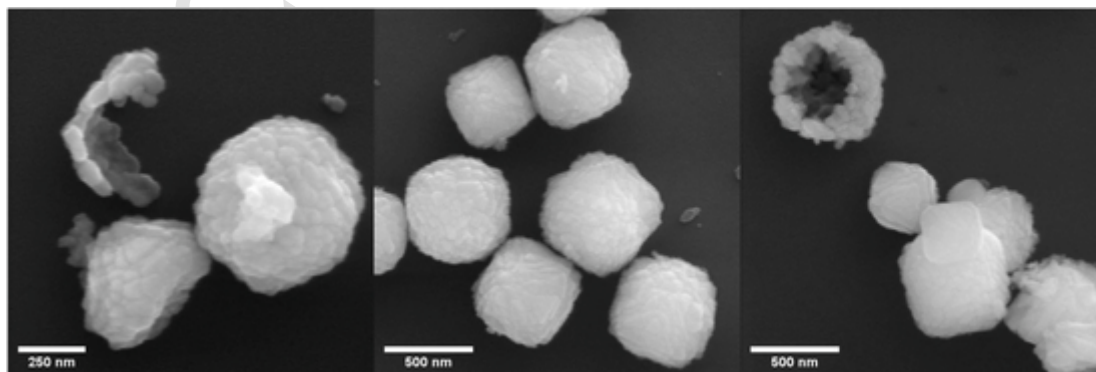


Fig. 3. SEM images of the as-prepared nanopowder ZnO₂; nanocrystals of 20–40 nm in diameter agglomerate in hollow microspheres or rounded cubes with diameters around 500 nm.

Table 1

Crystallographic parameters of nano-ZnO₂ obtained by Rietveld refinement. Space group *Pa* $\bar{3}$ (No. 205), the lattice parameter $a_0 = 4.89314(14)$ Å, the atomic displacement parameter B_{iso} , the weighted profile R-factor $R_{\text{wp}} = 2.35\%$, the expected R-factor $R_{\text{exp}} = 1.07\%$ and the goodness-of-fit $\chi^2 = 4.82$ [58].

Atom	Wyckoff position	Fractional coordinates			B_{iso} (Å ²)
		x	y	z	
Zn	4a	0	0	0	1.679(20)
O	8c	0.41309(27)	0.41309(27)	0.41309(27)	4.35(11)

tween the calculated and experimental diffraction patterns can only be seen for the most intense peaks of the diffraction pattern, but the peaks at higher scattering angles show excellent agreement with the experiment (see the inset in Fig. 2).

Crystallite size obtained from Rietveld refinement is $d = 22$ nm. Although the parameter responsible for the microstrain modeling was set to be refined, it converged to zero indicating that no microstrain is present in the sample. The crystallographic parameters obtained by refinement are reported in Table 1. Our experimental XRD pattern of ZnO₂ sample and crystallographic parameters agree well with the experimental data obtained for ZnO₂ nanopowder in the previous studies [11,30,31,57].

The insight into the morphology of the prepared ZnO₂ nanopowder was obtained by using SEM measurements. Fig. 3 shows hollow sphere or rounded-cube structures whose shells are composed of uniform ZnO₂ layered nanocrystals with a thickness of several tenths nanometers, the size of the structures is around 200–500 nm.

3.2. Optical absorption spectroscopy

The absorption spectrum of nano-ZnO₂ is shown in Fig. 4. The optical band gap was determined using absorbance (*A*) as a function of photon energy. The intersection between the extrapolation of the linear part of the curve and the axis $A = 0$ gives the optical band gap value of 4.6 eV. This value is in good agreement with the 4.5 eV value obtained using the same method by J.E. Morales-Mendoza et al. in Ref. [30]. The discrepancy is seen with the values (3.13–3.25 eV) reported in Ref. [20], however, this could be associated with the large porosity of the sample used in their research.

3.3. Infrared and Raman spectroscopy

The infrared spectrum (Fig. 5) of nano-ZnO₂ has four absorption bands in the far-infrared range at about 210, 274, 349 and 434 cm⁻¹ (Table 2).

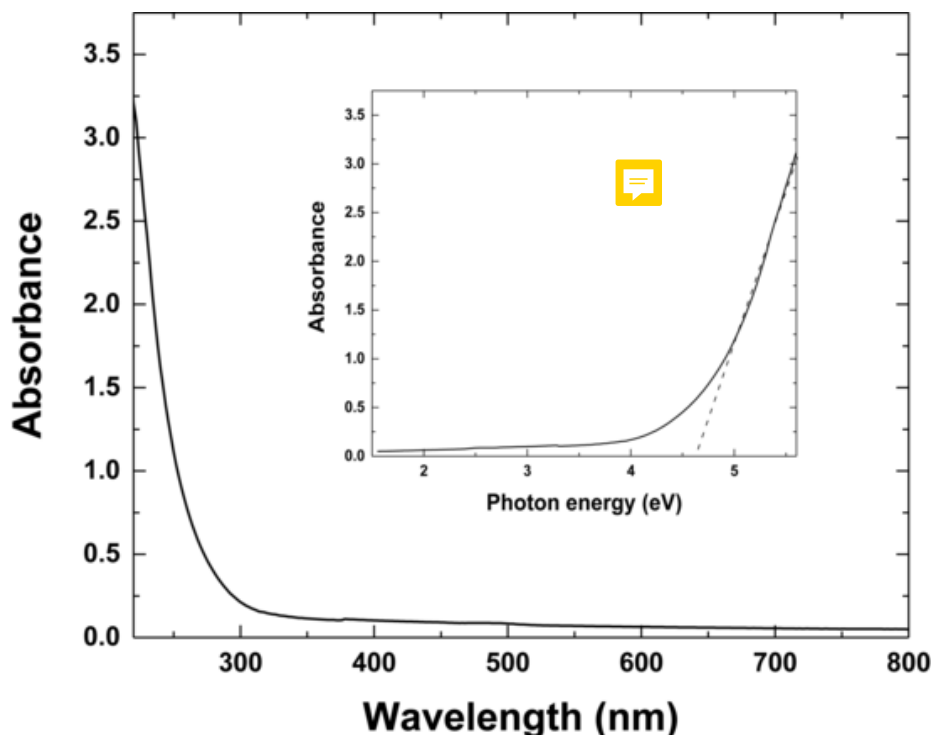


Fig. 4. Optical absorption of nano-ZnO₂. $(Ah\nu)^{1/2}$ as a function of $h\nu$ for the nanocrystalline ZnO₂.

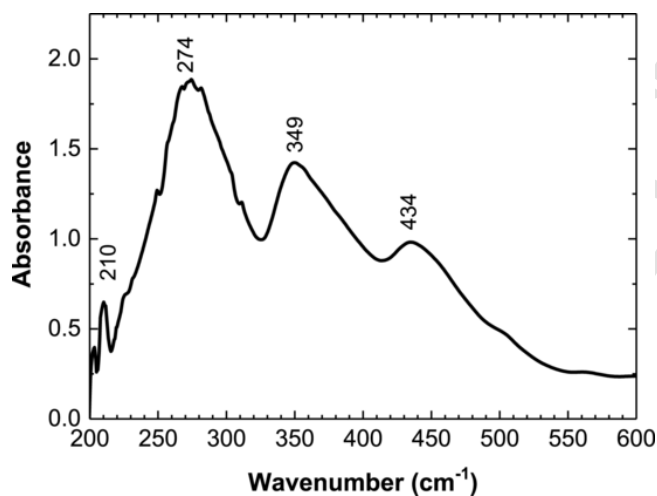


Fig. 5. The infrared spectrum of nano-ZnO₂ in the range of 200–600 cm⁻¹.

In-situ temperature-dependent Raman scattering spectra of nano-ZnO₂ (Fig. 6) were recorded on an as-prepared sample upon heating in air at the temperatures 120, 250 and 270 °C. Three bands due to the ZnO₂ phase were identified at 410, 471 and 838 cm⁻¹ in the Raman scattering spectrum up to 250 °C. Thermal decomposition of ZnO₂ to ZnO was observed at around ≈250 °C. At higher temperatures, three new bands of nanocrystalline ZnO were identified at 330, 436, 582 cm⁻¹ in agreement with the frequency values from Ref. [59].

3.4. X-ray absorption spectroscopy

X-ray absorption spectra of nano-ZnO₂ powder, measured at 10, 150, and 300 K, were analyzed using the reverse Monte Carlo (RMC) method based on the evolutionary algorithm (EA), implemented in the EvAX code [61]. The review of the method can be found in Ref. [62], and its recent application in the analysis of complex material

CuMo_{1-x}W_xO₄ in Refs. [63,64]. The use of the RMC method in the analysis of ZnO₂ EXAFS allowed us to extract reliable structural information for coordination shells up to 8 Å.

First, the extended X-ray absorption fine structures (EXAFS) $\chi(k)k^2$ (Fig. 7) were extracted using a conventional procedure [65]. Note the high quality of the obtained EXAFS with a large signal/noise ratio. Upon increasing temperature from 10 to 300 K, the EXAFS oscillations become damped at the high- k values due to thermal disorder. The structural contributions from coordination shells up to 8 Å are well visible in the Fourier transforms of EXAFS. The first two dominating peaks at 1.5 Å and 3.0 Å are mainly due to 6 oxygen atoms of the first coordination shell ($r(\text{Zn-O}_1) = 2.11$ Å) and 12 zinc atoms of the third coordination shell ($r(\text{Zn-Zn}_3) = 3.46$ Å), respectively. A more detailed interpretation of the EXAFS signals will be given below.

To perform RMC analysis of EXAFS, $4a_0 \times 4a_0 \times 4a_0$ simulation boxes (supercells) with periodic boundary conditions (PBC) were constructed, referencing the ZnO₂ (*Pa*3) crystallographic structure [11]. RMC/EA calculations were performed for 32 atomic configurations. At each iteration, the new atomic configuration was generated by randomly displacing all atoms in the simulation box with the maximally allowed shift of 0.4 Å to get the best possible agreement between the Morlet wavelet transforms (WTs) [66] of the experimental and calculated EXAFS spectra. The calculations were performed in the k -space range from 2.5 to 13 Å⁻¹ and in the R -space range from 0.8 to 7.5 Å. No significant improvement in the residual was observed after 5000 iterations. Note that there is a small difference between the positions R of the peaks in FTs and the crystallographic values r due to the phase shifts present in EXAFS.

The configuration-averaged EXAFS spectra were calculated by ab initio real-space multiple-scattering (MS) FEFF8.50L code [67], including the MS effects up to 8th order. The scattering potential and partial phase shifts were calculated only once within the muffin-tin (MT) approximation [68] for the cluster with a radius of 4.0 Å, centered at the absorbing Zn atom and constructed based on crystallographic ZnO₂ structure [11]. Small variations of the cluster potential due to atom displacements during the RMC/EA simulations were neglected. The photoelectron inelastic losses were accounted for within the one-plasmon ap-

Table 2

Comparison of the calculated and experimental frequencies of the phonon modes in ZnO₂.

Frequency (cm ⁻¹)			Symmetry	Activity	Types
Calculated		Experimental			
CRYSTAL	VASP	this study	other studies		
WC1LYP	PBE0	PBE0			
143.2	142.5	135.1	F _u	IR	Lattice
143.5	143.3	136.0	E _u		Lattice
151.9	153.2	147.3	A _u		Lattice
208.1	208.9	199.3	F _u	IR	Lattice
271.3	274.3	266.1	F _u	IR	Lattice
306.2	307.9	304.0	A _u		Lattice
342.5	347.1	338.7	F _u	IR	Lattice
369.6	374.7	364.8	E _u		Lattice
408.7	416.2	408.9	F _g	Raman	O ₂ ²⁻ libration
		410	[11], 410 [30], 414.2 [20], 411 [37], 410 [38], 410 [60]		
419.5	425.5	421.0	E _g	Raman	O ₂ ²⁻ libration
428.2	431.8	423.1	F _u	IR	Lattice
477.1	485.6	482.6	F _g	Raman	O ₂ ²⁻ libration
		471	483 [11], 476.3 [20], 473 [30], 472 [37], 478 [38], 475 [60]		
916.8	977.9	975.2	A _g	Raman	O ₂ ²⁻ stretching
		838	835 [11], 840.7 [20], 838 [30], 838 [37], 842 [38], 840 [60]		
918.6	978.7	974.9	F _g	Raman	O ₂ ²⁻ stretching
		1080.8	1080.8 [20], 871 [30], 936 [37], 960 [38], 937 [60]		

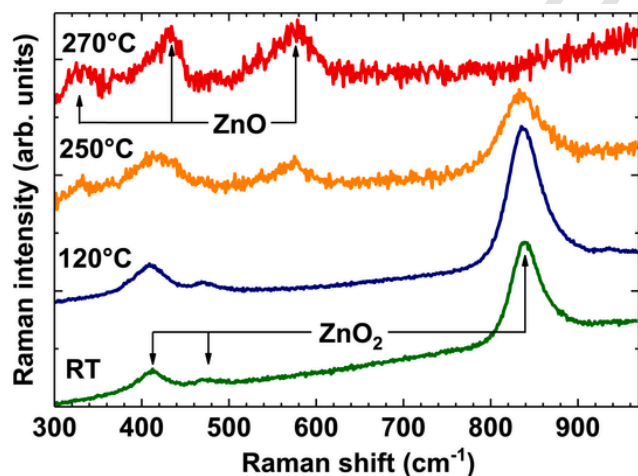


Fig. 6. Evolution of the Raman scattering spectrum of nano-ZnO₂ upon heating from room temperature to 270 °C.

proximation using the complex exchange-correlation Hedin-Lundqvist potential [69]. The amplitude reduction factor S_0^2 is included in the scattering amplitude [68], calculated by the FEFF code, and no additional correction of the EXAFS amplitude was performed.

The result of the RMC/EA analysis is shown in Fig. 8. The model reproduces well the experimental data in both k and R space at all temperatures, suggesting that the average structure determined by XRD gives a good starting model to fit the EXAFS data. An increase in tem-

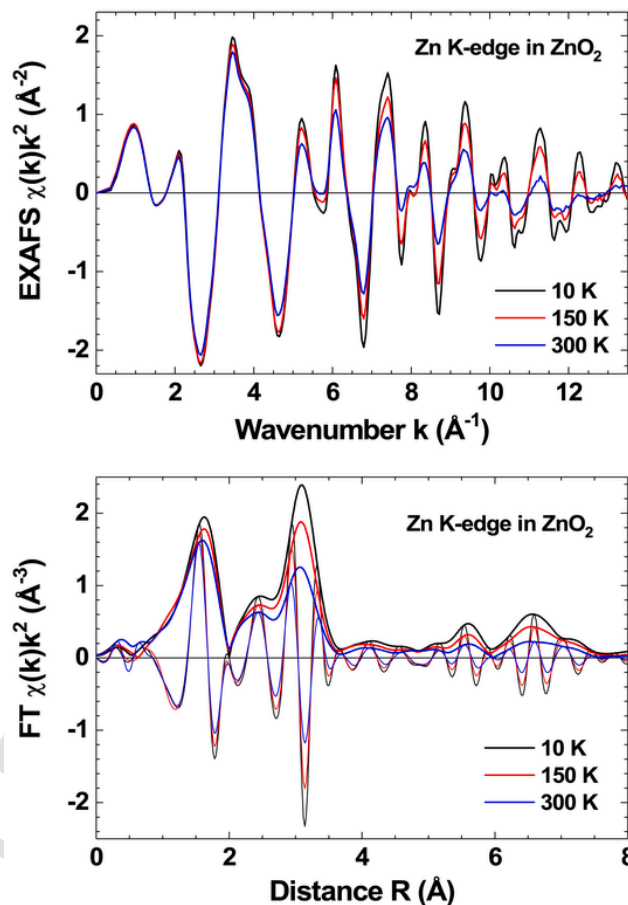


Fig. 7. Experimental Zn K-edge EXAFS $\chi(k)k^2$ spectra and their Fourier transforms (FTs) of nano-ZnO₂ at 10, 150 and 300 K. Note that the positions of peaks in the FTs were not corrected for the phase shift, therefore, they are located at slightly shorter than crystallographic distances.

perature from 10 to 300 K leads to an increase in thermal disorder, which more strongly affects peaks beyond the first coordination shell ($r > 2$ Å). Partial radial distribution functions (RDFs) $g_{\text{Zn-O}}(r)$ and $g_{\text{Zn-Zn}}(r)$ were calculated from the coordinates of atoms in the supercell and are shown in Fig. 9.

The atomic coordinates in the RMC simulation boxes were used to extract information on the mean-square displacements (MSDs) of atoms and the mean-square relative displacements (MSRDs) for atom pairs [61]. The MSRDs for Zn–O and Zn–Zn atom pairs were evaluated for the first three peaks, corresponding to the O₁, O₂, and Zn₃ coordination shells. The MSDs for oxygen and zinc atoms were also determined, taking into account the displacement of O and Zn atoms from their equilibrium positions.

The difference between MSRD_{AB} for the atom pair A–B and a sum of MSD_A and MSD_B gives the displacement correlation function (DCF) [70].

$$2\text{DCF}_{AB} = \text{MSRD}_{AB} - (\text{MSD}_A + \text{MSD}_B). \quad (1)$$

Note that at long distances the correlation of atomic motion vanishes and DCF = 0. This fact allows determining both MSRD and MSD factors from a single EXAFS spectrum when reliable analysis of distant coordination shells is possible [71]. The temperature dependence of the MSRD and MSD factors in ZnO₂ for the first three coordination shells is shown in Fig. 10. Weak variation of the MSRDs with increasing temperature indicates a rather strong bonding between Zn and nearest O and Zn atoms. Moreover, the near-neighbor atomic motions are strongly

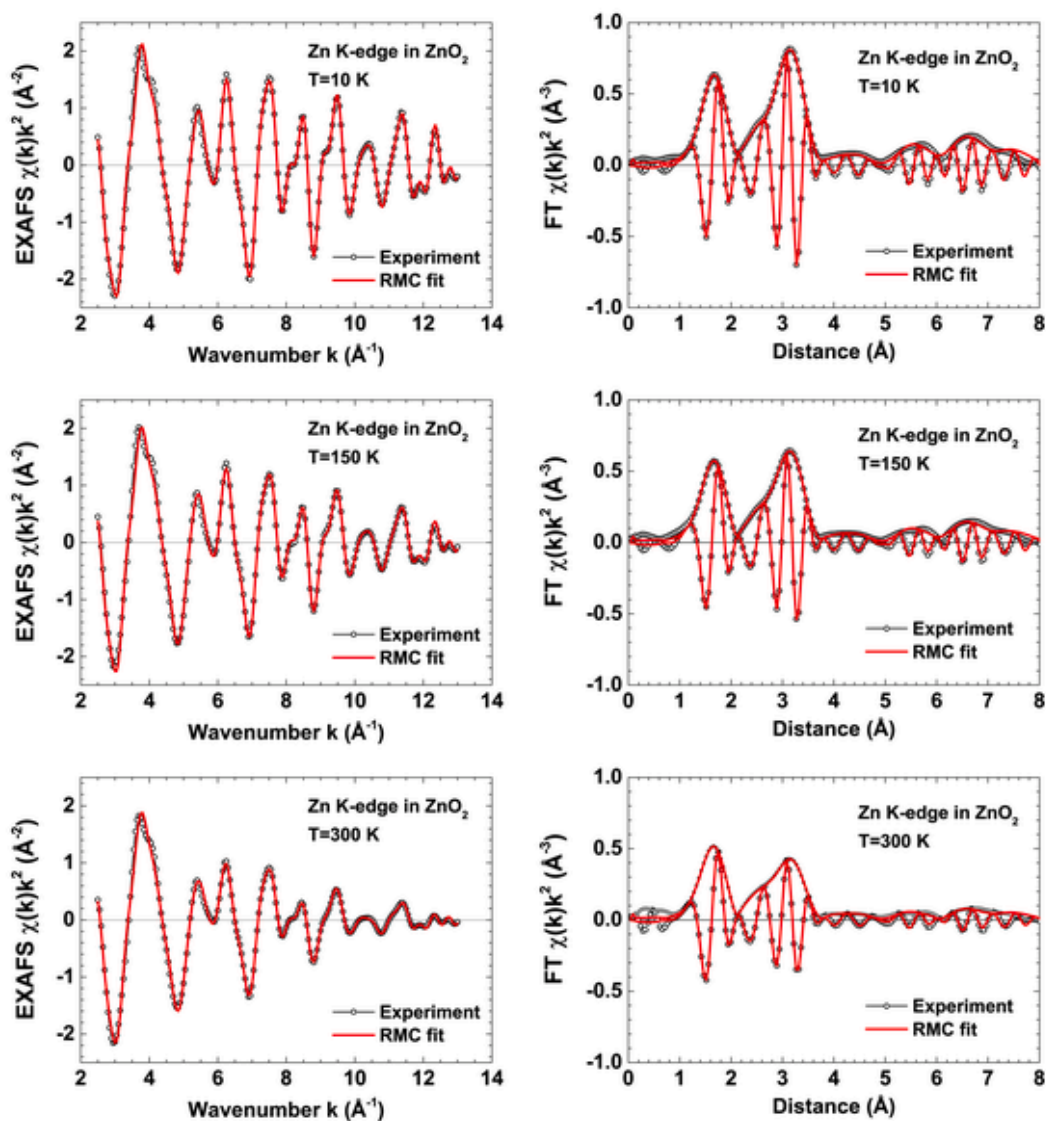


Fig. 8. Results of RMC/EA-EXAFS calculations for nano-ZnO₂ at 10 and 300 K: comparison of the experimental and calculated (RMC/EA) Zn K-edge EXAFS spectra $\chi(k)k^2$ (left panels) and their Fourier transforms (FTs) (right panels).

correlated, as evidenced by a large difference between MSRD factors and a sum of respective MSDs.

The thermal dependence of the MSRD factors was described by a sum of static and vibrational disorder contributions using the correlated Einstein model [72] (see dashed lines in Fig. 10). The characteristic Einstein temperatures θ_E were determined to be 400 K for Zn–O₁, 320 K for Zn–O₂, and 220 K for Zn–Zn₃ atom pairs. The static contribution to MSRDs was estimated to be about 0.005–0.006 Å².

3.5. First-principles calculations

Experimental studies are accompanied by ab initio quantum chemistry calculations which were performed using the method of a linear combination of atomic orbitals (LCAO) as realized in the CRYSTAL17 code [73]. For a complete representation, the calculations were also done using a plane wave (PW) approach as implemented in the VASP code [74,75].

Based on XRD data (Table 1), ZnO₂ was modelled using the crystallographic structure belonging to a space group No. 205 ($Z = 4$, ) with Zn atoms occupying Wyckoff position 4a, and O atoms located at position 8c, with a total of 12 atoms (4 Zn and 8 O) in the unit cell.

LCAO calculations, including analyses of phonon frequencies and vibration intensities, were performed using algorithms as implemented in CRYSTAL17 code [73,76–79]. All-electron atom-centered sets of Gaussian-type functions were used to describe atoms. For Zn, the (8s)(4111sp)(41d) basis set was adopted from Gryaznov et al. [80,81], while for O the (8s)(411sp)(1d) basis set was taken from Bredow et al. [82]. Having considered multiple formulations of the exchange-correlation functional of the DFT, we settled for WC1LYP, a 1-parameter functional that combines the WC exchange functional with 16% of Hartree-Fock exchange and the LYP correlation functional [83]. For the sake of comparing Gaussian basis set to a plane-wave basis set, we also include results obtained with the PBE0, a hybrid version of the PBE exchange-correlation functional with 25% of HF exchange [84]. Reciprocal space was sampled using a Monkhorst-Pack mesh [85] with a shrinking factor of 16, which yielded 249 points in the irreducible part of the Brillouin zone. The self-consistent field (SCF) convergence on the difference in total electronic energy was set to 10^{−10} hartree for geometry optimization and phonon frequency calculations. Additionally, we evaluated the values of the MSD parameters at different temperatures using tensors of anisotropic displacement parameters (ADP) obtained with a scheme described in Ref. [86] and implemented in the CRYSTAL17 code [73].

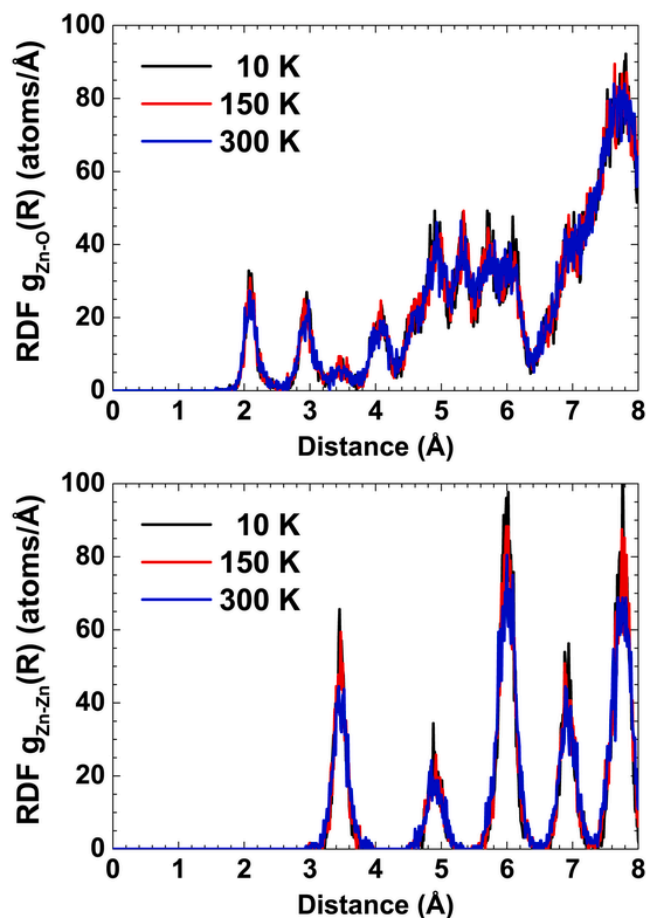


Fig. 9. Temperature dependence of the partial radial distribution functions (RDFs) $g_{\text{Zn-O}}$ and $g_{\text{Zn-Zn}}$ calculated from the results of RMC/EA simulations.

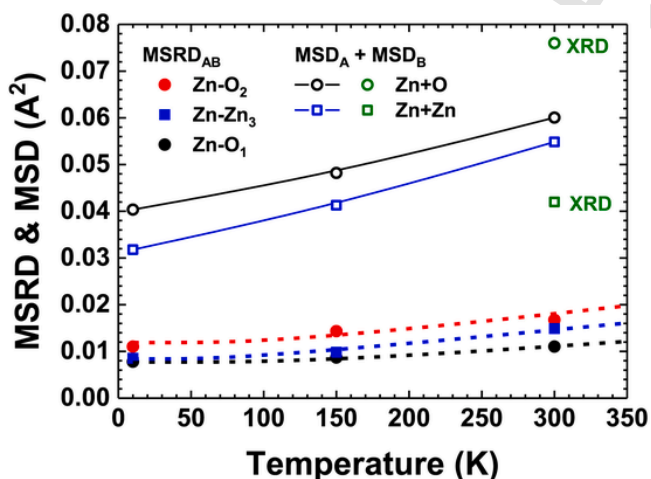


Fig. 10. Temperature dependence of the MSD (open symbols) and MSRD (solid symbols) factors in nano-ZnO₂ calculated from the results of RMC/EA simulations. The MSRD factors are given for the first three coordination shells of zinc (O₁, O₂ and Zn₃). Dashed lines correspond to the correlated Einstein models (see text for details). The MSD factors obtained by XRD at 300 K are also shown for comparison. The values of the MSD factors are given for a pair of atoms, i.e they are equal to the sum of MSD for Zn and O/Zn atoms.

The PW calculations using the Vienna ab initio simulation program VASP version 5.4.4 [74,75] were performed for a 12-atom ($1 \times 1 \times 1$) unit cell using a $4 \times 4 \times 4$ Γ -centered Monkhorst-Pack k-point mesh using the projector augmented wave (PAW) method. The valence electron configurations of the PAW pseudopotentials for Zn and O were ($3d^{10}, 4s^2$) and ($2s^2, 2p^4$), respectively. Cut-off energy of 600 eV for the expansion of the plane wave basis set was employed to ensure well-converged energies ($< 10^{-8}$ eV) and atomic forces ($< 10^{-3}$ eV/Å) for the structural relaxations and the phonon calculations. For a better comparison of the PW and LCAO approaches, hybrid functionals were used also in the calculations by VASP. An admixture of 25% (the default value for PBE0) and 20% of Hartree-Fock (HF) exact exchange α^{HF} were employed. The value of 20% shows the effect of an exact exchange reduction in comparison to the hybrid functional WC1LYP, which includes only 16% of HF exact exchange.

The calculated values of the band gap E^{gap} , the lattice parameter a_0 as well as the Zn-O and O-O bond distances for the fully relaxed ZnO₂ structure using both series of calculations (CRYSTAL17 and VASP) are reported in Table 3. Frequencies of the phonon modes are compared with the experimental data in Table 2. The MSD parameters calculated for three selected temperatures (0 K, 150 K, and 300 K) using the CRYSTAL17 code are given in Table 4.

3.6. Discussion

Nanocrystalline ZnO₂ synthesized in the present work is a wide-band gap (4.6 eV) insulator, and its crystallographic structure is influenced by the size effect. The structure was studied by two complementary techniques, XRD and EXAFS, which probe long-range and short-range orders, respectively. The lattice parameter a_0 of our sample (Table 1) corresponds well to that reported previously in the literature [11,30–32,57]. Its nanocrystalline nature (crystallite size $d = 22$ nm) appears as a broadening of Bragg peaks in the XRD pattern in Fig. 2 and leads to some crystal structure relaxation, which can be expected to be larger near the crystallite surface or around defects (for example, oxygen vacancies [17]) located within the crystallites. Such relaxation introduces static disorder into the regular crystal lattice and promotes a variation of interatomic distances leading to the broadening of peaks in the partial RDFs $g_{\text{Zn-O}}(r)$ and $g_{\text{Zn-Zn}}(r)$ in Fig. 9. The MSD factors can be evaluated from the atomic displacement parameters B_{iso} (Table 1) and are equal to $\text{MSD}_{\text{XRD}}(\text{Zn}) = 0.021 \text{ \AA}^2$ and $\text{MSD}_{\text{XRD}}(\text{O}) = 0.055 \text{ \AA}^2$.

Table 3

The band gap E^{gap} (in eV) and the lattice parameter a_0 as well as the Zn-O and O-O bond distances d^{ZnO} and d^{OO} (all in Å) obtained with the hybrid functionals PBE0 [84] and WC1LYP [83] for the fully relaxed ZnO₂ structure are listed. α^{HF} specifies the portion of exact exchange employed with actual hybrid functional compared with published experimental data for structure [11] and band gap [30,32,41].

Code	Functional	α^{HF}	a_0	d^{ZnO}	d^{OO}	E^{gap}
CRYSTAL	PBE0	0.25	4.889	2.106	1.479	5.39
	WC1LYP	0.16	4.902	2.109	1.502	4.23
VASP	PBE0	0.25	4.890	2.110	1.458	5.25
	PBE0	0.20	4.902	2.114	1.465	4.63
Experiment			4.893	2.109	1.473	3.8–4.6

Table 4

The sums of the MSD factors at different temperatures for the Zn + Zn and Zn + O atom pairs (in Å²) obtained from calculations using anisotropic displacement parameter tensor as implemented in CRYSTAL code.

Temperature	Zn + Zn	Zn + O
0 K	0.0024	0.0037
150 K	0.0038	0.0047
300 K	0.0066	0.0072

Note that they include contributions from a reduced crystallite size and thermal disorder.

SEM measurements show the complex structure of powder, visualizing the hollow spherical or rounded-cube shape of agglomerated particles with dimensions of about 200–500 nm. The surface of particles is formed by the mosaic structure of spliced nanoparticles with 20–40 nm diameter that is clearly seen from the layered particle in the upper left corner (left panel) in Fig. 3.

To distinguish thermal and static disorder, the temperature dependence of the obtained MSD factors for Zn–O and Zn–Zn atom pairs was described by the correlated Einstein model (dashed lines in Fig. 10), and the contribution of the static disorder was estimated to be about 50–60%. At the same time, the large difference between the sum of two MSD factors and the MSD factors indicates a significant amount of correlation in the vibrational motion of the nearest atoms.

Properties of calculated and experimentally observed ZnO₂ fundamental vibrations are listed in Table 2. Group theory predicts five IR-active and five Raman-active modes. Three distinct bands due to vibrations of O₂²⁻ anion are observed in the calculated Raman spectrum: a band consisting of two peaks around ~410–420 cm⁻¹ (O–O libration, a rotation along an axis perpendicular to the bond), a band at ~470–480 cm⁻¹ (libration), and the major band consisting of two peaks above 900 cm⁻¹ (O–O bond stretching).

Calculated vibrational modes of O₂²⁻ anion show localized nature and the anion behaves like a single particle, rather than allowing independence to its constituent atoms. All the molecular stretching and libration vibrations of O₂²⁻ anion are Raman-active. In all Raman-inactive vibrational modes, the O–O fragment moves as a rigid body (both atoms have identical translation vectors). In contrast, all Raman-active modes are comprised exclusively of translations that bend, stretch and rotate O–O bond relative to stationary Zn atoms. Conversely, the lattice vibrations are Raman-inactive and only a part of those are IR-active (Table 2).

Calculated vibration frequencies are in good agreement with the experimentally observed Raman and IR frequencies [11,20,30,37,38,60]. These results are in good relation to the performed measurements (410, 471 and 838 cm⁻¹). The experimental Raman spectra showed only one stretching band at 838 cm⁻¹ and two libration bands at 410 and 471 cm⁻¹ due to the overlap of broad Raman bands. They also agree with previously reported results: 840 cm⁻¹ attributed to O–O bond stretching [87]. Peaks at 835, 483, and 407 cm⁻¹ are reported by Escobedo-Morales et al. [11], with the first, most intense signal being attributed to the stretching of the O–O bond, while two other signals are left uninterpreted. Experimentally measured IR peaks at 210, 274, 349, and 434 cm⁻¹ are in good agreement with the calculated ones. The peak located at 434 cm⁻¹ was also previously reported in the literature [18,29]. The theoretically predicted IR band at 143 cm⁻¹ was not observed in our experiments due to the KBr pellet not being transparent in this region.

The experimental MSD parameters (Fig. 10) obtained by the RMC simulations from the Zn K-edge EXAFS can be compared with those calculated (Table 4) and estimated by XRD. The two sets of the calculated MSD parameters for Zn–O and Zn–Zn atom pairs differ significantly for each temperature with the experimental values being larger. The calculated MSD values include only vibrational contributions, whereas the static disorder present in the ZnO₂ nanoparticles dominates the experimental MSD values obtained from the EXAFS and XRD data. As a result, the calculated MSDs are an order of magnitude lower than the experimental ones. The MSD values obtained by RMC and XRD are in reasonable agreement taking into account the weak sensitivity of powder XRD data to the atomic displacement parameters B_{iso} (Table 1) [88].

4. Conclusions

A comprehensive study of nanocrystalline ZnO₂ has been performed using several experimental methods and first-principles calculations.

The sample was produced by a hydrothermal process using zinc acetate as a precursor and hydrogen peroxide as an oxidizing agent. Rietveld refinement of the X-ray diffraction pattern confirmed cubic-ZnO₂ structure belonging to the space group $Pa\bar{3}$ (205) with a short peroxide O–O bond distance (1.47 Å). The crystallite size was estimated to be about 22 nm. The indirect band gap of about 4.6 eV was found using optical absorption spectroscopy. High-resolution SEM images were taken to study ZnO₂ morphology.

The local atomic structure around zinc atoms was probed for the first time by the Zn K-edge EXAFS spectroscopy in combination with the reverse Monte Carlo simulations, which made it possible to determine the partial Zn–O and Zn–Zn RDFs. The analysis of partial RDFs $g_{\text{Zn-O}}(r)$ and $g_{\text{Zn-Zn}}(r)$ allowed us to estimate MSD factors for the Zn–O and Zn–Zn atom pairs and MSD factors of O and Zn atoms. Both MSD and MSDR factors have unusually large values, which were explained by the local structure relaxation due to the size effect. The large values of the MSD factors obtained by RMC are in reasonable agreement with those calculated from the atomic displacement parameters B_{iso} , obtained by the XRD method. The static and vibrational contributions to the MSDRs were separated using the correlated Einstein model, and the Einstein temperatures θ_E were determined for the three nearest coordination shells.

Thermal decomposition of ZnO₂ to wurtzite ZnO around 250 °C was observed by temperature-dependent Raman spectroscopy. Below 250 °C, the Raman spectrum of ZnO₂ is dominated by the libration and stretching vibrational modes of O₂²⁻ anion, whereas its far-infrared spectrum contains only lattice modes. The detailed analysis of the fundamental vibrations of the ideal ZnO₂ crystal was performed using the hybrid exchange density functional theory within the LCAO and plane wave approaches. Both theoretical models predicted the equilibrium geometries, wide-band gap, and phonon frequencies in good agreement with the experimental results. The temperature dependence and smallness of the calculated MSD factors compared to those obtained from the analysis of XRD and EXAFS confirmed the significant contribution of the static disorder to their experimental values.

CRediT author statement

Dmitry Bocharov: Conceptualization, Methodology, Validation, Formal analysis, Investigation, Data Curation, Writing - Original Draft, Writing - Review & Editing, Visualization, Supervision.

Andrei Chesnokov: Methodology, Formal analysis, Investigation, Data Curation, Writing - Review & Editing, Visualization.

George Chikvaidze: Formal analysis, Investigation, Writing - Review & Editing, Visualization.

Jevgenijs Gabrusenoks: Formal analysis, Investigation, Writing - Review & Editing, Visualization.

Reinis Ignatans: Investigation, Writing - Review & Editing, Visualization.

Robert Kalendarev: Investigation.

Matthias Krack: Methodology, Software, Formal analysis, Investigation, Resources, Data Curation, Writing - Review & Editing.

Karlis Kundzins: Investigation, Writing - Review & Editing, Visualization.

Alexei Kuzmin: Conceptualization, Methodology, Software, Validation, Formal analysis, Investigation, Writing - Review & Editing, Data Curation, Writing - Original Draft, Visualization, Supervision.

Nina Mironova-Ulmane: Formal analysis, Investigation, Writing - Review & Editing, Visualization.

Inga Pudza: Methodology, Software, Formal analysis, Investigation, Data Curation, Writing - Review & Editing, Visualization.

Laurits Puust: Investigation.

Ilmo Sildos: Investigation.

Evgeni Vasil'chenko: Investigation.

Martins Zubkins: Formal analysis, Investigation, Writing - Original Draft, Writing - Review & Editing, Visualization.

Juris Purans: Conceptualization, Methodology, Validation, Resources, Writing - Review & Editing, Supervision, Project administration, Project administration, Funding acquisition.

Declaration of competing interest

The authors declare that they have no known competing financial interests or personal relationships that could have appeared to influence the work reported in this paper

Acknowledgements

The authors are grateful to the staff of the PETRA-III P65 beamline for assistance during the experiment. Financial support was provided by ERAF Project Nr. 1.1.1.1/20/A/057. M.K. acknowledges access to Piz Daint at the Swiss National Supercomputing Centre, Switzerland (CSCS) under the PSI's share with the project ID psi01. The Institute of Solid State Physics, University of Latvia (Latvia) as the Centre of Excellence has received funding from the European Union's Horizon 2020 Framework Programme H2020-WIDESPREAD01-2016-2017-Teaming Phase2 under grant agreement No. 739508, project CAMART2.

References

- Ibarra, A. Marcos-Fernandez, M. Alzorric, Mechanistic approach to the curing of carboxylated nitrile rubber (XNBR) by zinc peroxide/zinc oxide, *Polymer* 43 (2002) 1649–1655, [https://doi.org/10.1016/S0032-3861\(01\)00734-0](https://doi.org/10.1016/S0032-3861(01)00734-0).
- S. Ohno, N. Aburatani, N. Ueda, Foam Products from a High-Melting Synthetic Resin, DE Patent 2914058..
- F.L. Meleney, Use of zinc peroxide in oral surgery, *Int. J. Orthod. Oral Surg.* 23 (1937) 932–940, [https://doi.org/10.1016/S1072-3498\(37\)80183-1](https://doi.org/10.1016/S1072-3498(37)80183-1).
- R. Hagel, K. Redecker, Use of zinc peroxide as oxidant for explosives and pyrotechnical mixtures, US Patent 4,363,679 (1982)..
- Y. Zhang, X. Wu, X.Y. Hu, R. Guo, Low-temperature synthesis of nanocrystalline ZnO by thermal decomposition of a "green" single-source inorganic precursor in air, *J. Cryst. Growth* 280 (2005) 250–254, <https://doi.org/10.1016/j.jcrysgro.2005.03.001>.
- M. Gondal, Q. Drmsh, Z. Yamani, T. Saleh, Synthesis of ZnO₂ nanoparticles by laser ablation in liquid and their annealing transformation into ZnO nanoparticles, *Appl. Surf. Sci.* 256 (2009) 298–304, <https://doi.org/10.1016/j.apsusc.2009.08.019>.
- M. Sun, W. Hao, C. Wang, T. Wang, A simple and green approach for preparation of ZnO₂ and ZnO under sunlight irradiation, *Chem. Phys. Lett.* 443 (2007) 342–346, <https://doi.org/10.1016/j.cplett.2007.06.098>.
- L. Rosenthal-Toib, K. Zohar, M. Alagem, Y. Tsur, Synthesis of stabilized nanoparticles of zinc peroxide, *Chem. Eng. J.* 136 (2008) 425–429, <https://doi.org/10.1016/j.cej.2007.07.071>.
- B. Chavillon, L. Cario, A. Renaud, F. Tessier, F. Cheviré, M. Boujtita, Y. Pellegrin, E. Blart, A. Smeigh, L. Hammarstrom, et al., P-type nitrogen-doped ZnO nanoparticles stable under ambient conditions, *J. Am. Chem. Soc.* 134 (2011) 464–470, <https://doi.org/10.1021/ja208044k>.
- S. Lindroos, M. Leskelä, Growth of zinc peroxide (ZnO₂) and zinc oxide (ZnO) thin films by the successive ionic layer adsorption and reaction–SILAR–technique, *Int. J. Inorg. Mater.* 2 (2000) 197–201, [https://doi.org/10.1016/S1466-6049\(00\)00017-9](https://doi.org/10.1016/S1466-6049(00)00017-9).
- A. Escobedo-Morales, R. Esparza, A. García-Ruiz, A. Aguilar, E. Rubio-Rosas, R. Pérez, Structural and vibrational properties of hydrothermally grown ZnO₂ nanoparticles, *J. Cryst. Growth* 316 (2011) 37–41, <https://doi.org/10.1016/j.jcrysgro.2010.12.057>.
- M. Ortega-López, A. Avila-García, M. Albor-Aguilera, V.S. Resendiz, Improved efficiency of the chemical bath deposition method during growth of ZnO thin films, *Mater. Res. Bull.* 38 (2003) 1241–1248, [https://doi.org/10.1016/S0025-5408\(03\)00083-7](https://doi.org/10.1016/S0025-5408(03)00083-7).
- N. Uekawa, N. Mochizuki, J. Kajiwara, F. Mori, Y.J. Wu, K. Kakegawa, Nonstoichiometric properties of zinc oxide nanoparticles prepared by decomposition of zinc peroxide, *Phys. Chem. Chem. Phys.* 5 (2003) 929–934, <https://doi.org/10.1039/B210990E>.
- Q. Drmsh, M. Gondal, Z. Yamani, T. Saleh, Spectroscopic characterization approach to study surfactants effect on ZnO₂ nanoparticles synthesis by laser ablation process, *Appl. Surf. Sci.* 256 (2010) 4661–4666, <https://doi.org/10.1016/j.apsusc.2010.02.068>.
- C.-C. Hsu, N.-L. Wu, Synthesis and photocatalytic activity of ZnO/ZnO₂ composite, *J. Photochem. Photobiol., A* 172 (2005) 269–274, <https://doi.org/10.1016/j.jphotochem.2004.12.014>.
- Q. Guo, Q. Zhang, H. Wang, Z. Zhao, ZnO₂-promoted ZnO as an efficient photocatalyst for the photoreduction of carbon dioxide in the presence of water, *Catal. Commun.* 103 (2018) 24–28, <https://doi.org/10.1016/j.catcom.2017.09.010>.
- H. Bai, X. Liu, Green hydrothermal synthesis and photoluminescence property of ZnO₂ nanoparticles, *Mater. Lett.* 64 (2010) 341–343, <https://doi.org/10.1016/j.matlet.2009.11.008>.
- S. Cheng, D. Yan, J. Chen, R. Zhuo, J. Feng, H. Li, H. Feng, P. Yan, Soft-template synthesis and characterization of ZnO₂ and ZnO hollow spheres, *J. Phys. Chem. C* 113 (2009) 13630–13635, <https://doi.org/10.1021/jp9036028>.
- S. Chawla, H. Uppal, M. Yadav, N. Bahadur, N. Singh, Zinc peroxide nanomaterial as an adsorbent for removal of Congo red dye from waste water, *Ecotoxicol. Environ. Saf.* 135 (2017) 68–74, <https://doi.org/10.1016/j.ecoenv.2016.09.017>.
- D.A. Giannakoudakis, M. Florent, R. Wallace, J. Secor, C. Karwacki, T.J. Bandosz, Zinc peroxide nanoparticles: surface, chemical and optical properties and the effect of thermal treatment on the detoxification of mustard gas, *Appl. Catal., B* 226 (2018) 429–440, <https://doi.org/10.1016/j.apcatb.2017.12.068>.
- W.A. E-S, M. Mohamed, A.S. H. A. Sameh, N. Somaia, Antibacterial potential of a newly synthesized zinc peroxide nanoparticles (ZnO₂-NPs) to combat biofilm-producing multi-drug resistant *Pseudomonas aeruginosa*, *Egypt, J. Bot.* 59 (2019) 657–666, <https://doi.org/10.21608/ejbo.2019.7062.1277>.
- C. Bergs, L. Brück, R.R. Rosencrantz, G. Conrads, L. Elling, A. Pich, Biofunctionalized zinc peroxide (ZnO₂) nanoparticles as active oxygen sources and antibacterial agents, *RSC Adv.* 7 (2017) 38998–39010, <https://doi.org/10.1039/C7RA06332F>.
- H. Hu, L. Yu, X. Qian, Y. Chen, B. Chen, Y. Li, Chemoreactive nanotherapeutics by metal peroxide based nanomedicine, *Adv. Sci.* 8 (2021) 2000494, <https://doi.org/10.1002/advs.202000494>.
- W. Sun, F. Wang, B. Zhang, M. Zhang, V. Küpers, X. Ji, C. Theile, P. Bieker, K. Xu, C. Wang, M. Winter, A rechargeable zinc-air battery based on zinc peroxide chemistry, *Science* 371 (2021) 46–51, <https://doi.org/10.1126/science.abb9554>.
- F.M. Simanjuntak, S. Chandrasekaran, C.-C. Lin, T.-Y. Tseng, ZnO₂/ZnO bilayer switching film for making fully transparent analog memristor devices, *APL Materials* 7 (2019) 051108, <https://doi.org/10.1063/1.5092991>.
- P. Rawat, Shalu, R. Nagarajan, Mechanochemical transformation of ZnO₂ to highly defective ZnO, *Mater. Lett.* 212 (2018) 178–181, <https://doi.org/10.1016/j.matlet.2017.10.096>.
- N.P. Herring, L.S. Panchakarla, M.S. El-Shall, P-type nitrogen-doped ZnO nanostructures with controlled shape and doping level by facile microwave synthesis, *Langmuir* 30 (2014) 2230–2240, <https://doi.org/10.1021/la404593w>.
- V. Alvarado-Pérez, L.I. Cabrera-Lara, G. López-Téllez, D. Mendoza-Anaya, S. Hernández-López, M. Camacho-López, ZnO to ZnO₂ transformation assisted by H₂O₂ at ambient conditions, *Mater. Chem. Phys.* 233 (2019) 180–184, <https://doi.org/10.1016/j.matchemphys.2019.05.066>.
- S. Verma, S.L. Jain, Nanosized zinc peroxide (ZnO₂): a novel inorganic oxidant for the oxidation of aromatic alcohols to carbonyl compounds, *Inorg. Chem. Front.* 1 (2014) 534–539, <https://doi.org/10.1039/C3QI00092C>.
- J.E. Morales-Mendoza, F. Paraguay-Delgado, J.D. Moller, G. Herrera-Pérez, N. Pariona, Structure and optical properties of ZnO and ZnO₂ nanoparticles, *J. Nano Res.* 56 (2019) 49–62, <https://doi.org/10.4028/www.scientific.net/JNanoR.56.49>.
- J.L.L.D. Ramírez, V. Villegas, S. Sicairos, E. Guevara, M.B. Perea, B. Sánchez, Synthesis and characterization of zinc peroxide nanoparticles for the photodegradation of nitrobenzene assisted by UV-light, *Catalysts* 10 (2020) 1041, <https://doi.org/10.3390/catal10091041>.
- W. Chen, Y. Lu, M. Wang, L. Kroner, H. Paul, H. Fecht, J. Bednarcik, K. Stahl, Z. Zhang, U. Wiedwald, et al., Synthesis, thermal stability and properties of ZnO₂ nanoparticles, *J. Phys. Chem. C* 113 (2009) 1320, <https://doi.org/10.1021/jp808714v>.
- P. Chen, F. Sun, W. Wang, F. Tan, X. Wang, X. Qiao, Facile one-pot fabrication of ZnO₂ particles for the efficient fenton-like degradation of tetracycline, *J. Alloys Compd.* 834 (2020) 155220, <https://doi.org/10.1016/j.jallcom.2020.155220>.
- X. Han, R. Liu, W. Chen, Z. Xu, Properties of nanocrystalline zinc oxide thin films prepared by thermal decomposition of electrodeposited zinc peroxide, *Thin Solid Films* 516 (2008) 4025–4029, <https://doi.org/10.1016/j.tsf.2007.08.006>.
- A. Valour, F. Cheviré, F. Tessier, F. Grasset, B. Dierre, T. Jiang, E. Faulques, L. Cario, S. Jobic, Preparation of nitrogen doped zinc oxide nanoparticles and thin films by colloidal route and low temperature nitridation process, *Solid State Sci.* 54 (2016) 30–36, <https://doi.org/10.1016/j.solidstatesciences.2015.12.009>.
- M. Zubkins, J. Gabrusenoks, G. Chikvaidze, I. Aulika, J. Butikova, R. Kalendarev, L. Bikse, Amorphous ultra-wide bandgap ZnO_x thin films deposited at cryogenic temperatures, *J. Appl. Phys.* 128 (2020) 215303, <https://doi.org/10.1063/5.0028901>.
- G. Feng, L. Yang, T. Wang, J. Zhang, T. Lou, Hydrothermal preparation of nanocrystalline ZnO₂, *Particuology* 10 (2012) 388–391, <https://doi.org/10.1016/j.partic.2011.06.010>.
- H. Palma-Palma, M. Camacho-López, M.A. Camacho-López, A. Vilchis-Néstor, Preparation of zinc peroxide nanoparticles by laser ablation of solid in liquids, *Superficies y vacío* 28 (2015) 74–77.
- T. Daley, E. Raj, S. Ramos, G. Cibin, A. Dent, T.I. Hyde, G. Sankar, Tracking the formation of nano-sized zinc oxide from zinc peroxide by in situ XAS and XRD, *J. Phys.: Conf. Ser.* 430 (2013) 012080, <https://doi.org/10.1088/1742-6596/430/1/012080>.
- N. Vannerberg, Formation and structure of zinc peroxide, *Ark. Kemi.* 14 (1959) 119–124.
- D. Yang, M.A. Gondal, Z.H. Yamani, U. Baig, X. Qiao, G. Liu, Q. Xu, D. Xiang, J. Mao,

- K. Shen, 532 nm nanosecond pulse laser triggered synthesis of ZnO₂ nanoparticles via a fast ablation technique in liquid and their photocatalytic performance, *Mater. Sci. Semicond. Process.* 57 (2017) 124–131, <https://doi.org/10.1016/j.mssp.2016.09.043>.
- [42] K.-A. Kim, J.-R. Cha, M.-S. Gong, J.-G. Kim, Preparation of ZnO₂ nanoparticles using organometallic zinc (II) isobutylcarbamate in organic solvent, *Bull. Kor. Chem. Soc.* 35 (2014) 431–435, <https://doi.org/10.5012/bkcs.2014.35.2.431>.
- [43] C. Bergs, P. Simon, Y. Prots, A. Pich, Ultrasmall functional ZnO₂ nanoparticles: synthesis, characterization and oxygen release properties, *RSC Adv.* 6 (2016) 84777–84786, <https://doi.org/10.1039/C6RA16009C>.
- [44] R. Thapa, S. Ghosh, S. Sinthika, E. Mathan Kumar, N. Park, Magnetic, elastic and optical properties of zinc peroxide (ZnO₂): first principles study, *J. Alloys Compd.* 620 (2015) 156–163, <https://doi.org/10.1016/j.jallcom.2014.09.118>.
- [45] L.-S. Zhao, Y. Wang, C.-P. Chen, L.-L. Liu, H.-X. Yu, Y. Zhang, Y. Chen, X.-C. Wang, Elastic, electronic and optical properties of stable pentagonal ZnO₂, *Phys. E* 91 (2017) 82–87, <https://doi.org/10.1016/j.physe.2017.03.017>.
- [46] N. Wang, H. Zhang, S.-L. Wang, Y.-Z. Zhang, Room temperature ferromagnetism and visible light absorption of Fe-doped penta-ZnO₂ monolayer: first-principles calculations, *Chem. Phys. Lett.* 754 (2020) 137729, <https://doi.org/10.1016/j.cplett.2020.137729>.
- [47] H. Zhang, N. Wang, S. Wang, Y. Zhang, Effect of doping 3d transition metal (Fe, Co, and Ni) on the electronic, magnetic and optical properties of pentagonal ZnO₂ monolayer, *Physica E Low Dimens. Syst. Nanostruct.* 117 (2020) 113806, <https://doi.org/10.1016/j.physe.2019.113806>.
- [48] S. Guang-Lin, H. Hong-Mei, L. Yan-Ling, The stable or metastable phases in compressed Zn-O systems, *Chin. Phys. Lett.* 33 (2016) 026104, <https://doi.org/10.1088/0256-307X/33/2/026104>.
- [49] A. Bouibes, A. Zaoui, W. Luo, R. Ahuja, Promising optical characteristics of zinc peroxide from first-principles investigation, *Solid State Commun.* 263 (2017) 6–9, <https://doi.org/10.1016/j.ssc.2017.06.012>.
- [50] A. Bouibes, A. Zaoui, Investigating new polyphorms of Zn–O from variable composition, *Solid State Commun.* 220 (2015) 36–38, <https://doi.org/10.1016/j.ssc.2015.07.004>.
- [51] S.V. Nistor, L.C. Nistor, M. Stefan, D. Ghica, G. Aldica, J.N. Barascu, Crystallization of disordered nanosized ZnO formed by thermal decomposition of nanocrystalline hydrozincite, *Cryst. Growth Des.* 11 (2011) 5030–5038, <https://doi.org/10.1021/cg2009286>.
- [52] A. Uklein, V. Multian, G. Kuz'micheva, R. Linnik, V. Lisnyak, A. Popov, V.Y. Gayvoronsky, Nonlinear optical response of bulk ZnO crystals with different content of intrinsic defects, *Opt. Mater.* 84 (2018) 738–747, <https://doi.org/10.1016/j.optmat.2018.08.001>.
- [53] J. Purans, A. Menushenkov, S. Besedin, A.I.V. Minkov, I. Pudza, A. Kuzmin, K. Klementiev, S. Pascarelli, O. Mathon, A. Rosa, T. Irifune, M. Erements, Local electronic structure rearrangements and strong anharmonicity in YH₃ under pressures up to 180 GPa, *Nat. Commun.* 12 (2021) 1765, <https://doi.org/10.1038/s41467-021-21991-x>.
- [54] E. Welter, R. Chernikov, M. Herrmann, R. Nemausat, A beamline for bulk sample x-ray absorption spectroscopy at the high brilliance storage ring PETRA III, *AIP Conf. Proc.* 2054 (2019) 040002, <https://doi.org/10.1063/1.5084603>.
- [55] T. Taut, R. Kleeberg, J. Bergmann, Seifert Software: the new Seifert Rietveld program BGMN and its application to quantitative phase analysis, *Mater. Struct.* (1998) 57–66.
- [56] N. Doebelein, R. Kleeberg, Profex: a graphical user interface for the Rietveld refinement program BGMN, *J. Appl. Crystallogr.* 48 (2015) 1573–1580, <https://doi.org/10.1107/S1600576715014685>.
- [57] A. García-Ruiz, M. Aguilar, A. Aguilar, A. Escobedo-Morales, R. Esparza, R. Pérez, Rietveld structure refinement of hydrothermally grown zinc peroxide nanoparticles, *Mater. Res. Symp. Proc.* 1242. doi:10.1557/PROC-1242-S4-P114..
- [58] B.H. Toby, R factors in Rietveld analysis: how good is good enough?, *Powder Diffr.* 21 (2006) 67–70, <https://doi.org/10.1154/1.2179804>.
- [59] K.A. Alim, V.A. Fonoberov, M. Shamsa, A.A. Balandin, Micro-Raman investigation of optical phonons in ZnO nanocrystals, *J. Appl. Phys.* 97 (2005) 124313, <https://doi.org/10.1063/1.1944222>.
- [60] A. Escobedo-Morales, D. Téllez-Flores, M. de Lourdes Ruiz Peralta, J. Garcia-Serrano, A.M. Herrera-González, E. Rubio-Rosas, E. Sánchez-Mora, O. Olivares Xometl, Green method for producing hierarchically assembled pristine porous ZnO nanoparticles with narrow particle size distribution, *Mater. Chem. Phys.* 151 (2015) 282–287, <https://doi.org/10.1016/j.matchemphys.2014.11.067>.
- [61] J. Timoshenko, A. Kuzmin, J. Purans, EXAFS study of hydrogen intercalation into ReO₃ using the evolutionary algorithm, *J. Phys. Condens. Matter* 26 (2014) 055401, <https://doi.org/10.1088/0953-8984/26/5/055401>.
- [62] A. Kuzmin, J. Timoshenko, A. Kalinko, I. Jonane, A. Anspoks, Treatment of disorder effects in X-ray absorption spectra beyond the conventional approach, *Radiat. Phys. Chem.* 175 (2020) 108112, <https://doi.org/10.1016/j.radphyschem.2018.12.032>.
- [63] I. Jonane, A. Anspoks, G. Aquilanti, A. Kuzmin, High-temperature X-ray absorption spectroscopy study of thermochromic copper molybdate, *Acta Mater.* 179 (2019) 26–35, <https://doi.org/10.1016/j.actamat.2019.06.034>.
- [64] I. Jonane, A. Cintins, A. Kalinko, R. Chernikov, A. Kuzmin, Low temperature X-ray absorption spectroscopy study of CuMoO₄ and CuMo_{0.90}W_{0.10}O₄ using reverse Monte-Carlo method, *Radiat. Phys. Chem.* 175 (2020) 108411, <https://doi.org/10.1016/j.radphyschem.2019.108411>.
- [65] A. Kuzmin, J. Chaboy, EXAFS and XANES analysis of oxides at the nanoscale, *IUCrJ* 1 (2014) 571–589, <https://doi.org/10.1107/S2052252514021101>.
- [66] J. Timoshenko, A. Kuzmin, Wavelet data analysis of EXAFS spectra, *Comput. Phys. Commun.* 180 (2009) 920–925, <https://doi.org/10.1016/j.cpc.2008.12.020>.
- [67] A.L. Ankudinov, B. Ravel, J.J. Rehr, S.D. Conradson, Real-space multiple-scattering calculation and interpretation of X-ray-absorption near-edge structure, *Phys. Rev. B* 58 (1998) 7565–7576, <https://doi.org/10.1103/PhysRevB.58.7565>.
- [68] J.J. Rehr, R.C. Albers, Theoretical approaches to x-ray absorption fine structure, *Rev. Mod. Phys.* 72 (2000) 621, <https://doi.org/10.1103/RevModPhys.72.621>.
- [69] L. Hedin, B.I. Lundqvist, Explicit local exchange-correlation potentials, *J. Phys. C Solid State Phys.* 4 (1971) 2064–2083, <https://doi.org/10.1088/0022-3719/4/14/022>.
- [70] G. Beni, P.M. Platzman, Temperature and polarization dependence of extended x-ray absorption fine-structure spectra, *Phys. Rev. B* 14 (1976) 1514–1518, <https://doi.org/10.1103/PhysRevB.14.1514>.
- [71] I. Jonane, A. Anspoks, A. Kuzmin, Advanced approach to the local structure reconstruction and theory validation on the example of the WL₃-edge extended x-ray absorption fine structure of tungsten, *Model. Simulat. Mater. Sci. Eng.* 26 (2018) 025004, <https://doi.org/10.1088/1361-651x/aa9bab>.
- [72] E. Sevillano, H. Meuth, J.J. Rehr, Extended x-ray absorption fine structure debye-waller factors. i. monatomic crystals, *Phys. Rev. B* 20 (1979) 4908–4911, <https://doi.org/10.1103/PhysRevB.20.4908>.
- [73] R. Dovesi, V.R. Saunders, C. Roetti, R. Orlando, C.M. Zicovich-Wilson, F. Pascale, B. Cavalleri, K. Doll, N.M. Harrison, L.J. Bush, P. D'Arco, M. Llunell, M. Causà, Y. Noël, L. Maschio, A. Erba, M. Rerat, S. Casassa, CRYSTAL17 User's Manual, University of Torino, Torino, 2017.
- [74] G. Kresse, J. Furthmüller, Efficient iterative schemes for *ab initio* total-energy calculations using a plane-wave basis set, *Phys. Rev. B* 54 (1996) 11169–11186, <https://doi.org/10.1103/physrevb.54.11169>.
- [75] G. Kresse, D. Joubert, From ultrasoft pseudopotentials to the projector augmented-wave method, *Phys. Rev. B* 59 (1999) 1758–1775, <https://doi.org/10.1103/physrevb.59.1758>.
- [76] R. Dovesi, A. Erba, R. Orlando, C.M. Zicovich-Wilson, B. Cavalleri, L. Maschio, M. Rérat, S. Casassa, J. Baima, S. Salustro, B. Kirtman, Quantum-mechanical condensed matter simulations with CRYSTAL, *WIREs Comput. Mol. Sci.* 8 (2018) e1360, <https://doi.org/10.1002/wcms.1360>.
- [77] L. Maschio, B. Kirtman, R. Orlando, M. Rérat, *Ab Initio* analytical infrared intensities for periodic systems through a coupled perturbed Hartree-Fock/Kohn-Sham method, *J. Chem. Phys.* 137 (2012) 204113, <https://doi.org/10.1063/1.4767438>.
- [78] F. Pascale, C.M. Zicovich-Wilson, F. López Gejo, B. Cavalleri, R. Orlando, R. Dovesi, The calculation of the vibrational frequencies of crystalline compounds and its implementation in the CRYSTAL code: crystalline Compounds and the CRYSTAL Code, *J. Comput. Chem.* 25 (2004) 888–897, <https://doi.org/10.1002/jcc.20019>.
- [79] C.M. Zicovich-Wilson, F. Pascale, C. Roetti, V.R. Saunders, R. Orlando, R. Dovesi, Calculation of the vibration frequencies of α -quartz: the effect of Hamiltonian and basis set, *J. Comput. Chem.* 25 (2004) 1873–1881, <https://doi.org/10.1002/jcc.20120>.
- [80] D. Gryaznov, E. Blokhin, A. Sorokine, E.A. Kotomin, R.A. Evarestov, A. Bussmann-Holder, J. Maier, A comparative *ab initio* thermodynamic study of oxygen vacancies in ZnO and SrTiO₃: emphasis on phonon contribution, *J. Phys. Chem. C* 117 (2013) 13776–13784, <https://doi.org/10.1021/jp400609e>.
- [81] A. Chesnokov, D. Gryaznov, N.V. Skorodumova, E.A. Kotomin, A. Zitolo, M. Zubkins, A. Kuzmin, A. Anspoks, J. Purans, The local atomic structure and thermoelectric properties of Ir-doped ZnO: hybrid DFT calculations and XAS experiments, *J. Mater. Chem. C* (2021) 4948–4960, <https://doi.org/10.1039/D1TC00223F>.
- [82] T. Bredow, K. Jug, R.A. Evarestov, Electronic and magnetic structure of ScMnO₃: electronic and magnetic structure of ScMnO₃, *Phys. Status Solidi B* 243 (2006) R10–R12, <https://doi.org/10.1002/pssb.200541403>.
- [83] R. Demichelis, B. Cavalleri, M. Ferrabone, R. Dovesi, On the performance of eleven DFT functionals in the description of the vibrational properties of aluminosilicates: performance of eleven DFT functionals, *Int. J. Quant. Chem.* 110 (2010) 406–415, <https://doi.org/10.1002/qua.22301>.
- [84] C. Adamo, V. Barone, Toward reliable density functional methods without adjustable parameters: the PBE0 model, *J. Chem. Phys.* 110 (1999) 6158–6170, <https://doi.org/10.1063/1.478522>.
- [85] H.J. Monkhorst, J.D. Pack, Special points for Brillouin-zone integrations, *Phys. Rev. B* 13 (1976) 5188–5192, <https://doi.org/10.1103/PhysRevB.13.5188>.
- [86] A. Erba, M. Ferrabone, R. Orlando, R. Dovesi, Accurate dynamical structure factors from *ab initio* lattice dynamics: the case of crystalline silicon, *J. Comput. Chem.* 34 (2013) 346–354, <https://doi.org/10.1002/jcc.23138>.
- [87] N. Uekawa, N. Mochizuki, J. Kajiwara, F. Mori, Y.J. Wu, K. Kakegawa, Nonstoichiometric properties of zinc oxide nanoparticles prepared by decomposition of zinc peroxide, *Phys. Chem. Mater. Phys.* 5 (2003) 929–934, <https://doi.org/10.1039/b210990e>.
- [88] R.J. Hill, Rietveld refinement round robin. I. Analysis of standard X-ray and neutron data for PbSO₄, *J. Appl. Crystallogr.* 25 (1992) 589–610, <https://doi.org/10.1107/S0021889892003649>.